

# A locking-free face-centred finite volume (FCFV) method for linear elasticity

Ruben Sevilla

Zienkiewicz Centre for Computational Engineering,  
College of Engineering, Swansea University, Wales, UK

Matteo Giacomini, and Antonio Huerta

Laboratori de Càlcul Numèric (LaCàN),  
ETS de Ingenieros de Caminos, Canales y Puertos,  
Universitat Politècnica de Catalunya, Barcelona, Spain

June 21, 2018

## Abstract

A face-centred finite volume (FCFV) method is proposed for the linear elasticity equation. The FCFV is a mixed hybrid formulation, featuring a system of first-order equations, that defines the unknowns on the faces (edges in two dimensions) of the mesh elements. The symmetry of the stress tensor is strongly enforced using the well-known Voigt notation and the displacement and stress fields inside each cell are obtained element-wise by means of explicit formulas. The resulting FCFV method is robust and locking-free in the nearly incompressible limit. Numerical experiments in two and three dimensions show optimal convergence of the displacement and the stress fields without any reconstruction. Moreover, the accuracy of the FCFV method is not sensitive to mesh distortion and stretching. Classical benchmark tests including Kirch's plate and Cook's membrane problems in two dimensions as well as three dimensional problems involving shear phenomena, pressurised thin shells and complex geometries are presented to show the capability and potential of the proposed methodology.

**Keywords:** finite volume, face-centred finite volume, mixed hybrid formulation, linear elasticity, locking-free, hybridisable discontinuous Galerkin

## 1 Introduction

Despite the finite volume method (FVM) was originally proposed in the context of hyperbolic systems of conservation laws [26, 35], there has been a growing interest towards

its application to other physical problems, including the simulation of deformable structures [16, 47]. Several robust and efficient implementations of the FVM are available in both open-source and commercial libraries, making it an extremely attractive approach for industrialists.

The existing finite volume paradigms discussed in the structural mechanics community can be classified into two families, depending on the localisation of the unknowns in the computational mesh: the cell-centred finite volume (CCFV) method [4, 11, 22, 25] defines the unknowns at the centroid of the mesh elements, whereas the vertex-centred finite volume (VCFV) strategy [40, 42, 49] sets the unknowns at the mesh nodes. A major limitation of the CCFV method is the poor approximation of the gradient of the displacements at the faces using unstructured meshes [2, 7]. To overcome this issue, Jasak and Weller [23] proposed a correction to match the value of the gradient of the displacements on the faces to the neighbouring cells. More recently, Nordbotten and co-workers enriched the classical CCFV formulation with a discrete expression of the stresses on the mesh faces [32, 33] and the resulting multi-point stress approximation was shown to improve the description of the stresses at the interface between two cells. Similar drawbacks are experienced by the VCFV strategy which also requires a reconstruction of the gradient of the displacements to guarantee the first-order convergence of the stresses. Within this context, the accuracy of the reconstruction may suffer from the non-orthogonality of the mesh and poor approximations may result from the use of highly deformed grids.

Another critical aspect in the numerical treatment of linear elasticity problems is represented by the fulfilment of the balance of angular momentum which implies the symmetry of the stress tensor [5]. Starting from the pioneering work of Fraeijis de Veubeke [19], finite element formulations with weakly enforced symmetry of the stress tensor have been extensively studied in the literature [6]. In [24], the weak imposition of the symmetry of the stress tensor is investigated in the context of a cell-centred finite volume paradigm.

Recently, a face-centred finite volume (FCFV) method which defines the unknowns over the faces of the mesh elements has been introduced for Poisson and Stokes problems [36]. In the present work, the FCFV method is extended to simulate the behaviour of deformable bodies under the assumption of small displacements. Starting from the hybridisable discontinuous Galerkin (HDG) method by Cockburn and co-workers [8, 9, 20, 41], the discrete finite volume system is derived by setting a constant degree of approximation in the recently proposed HDG formulation of the linear elasticity equation based on Voigt notation [37]. The resulting finite volume strategy involves the solution of a symmetric system of equations to determine the displacements on the mesh faces (edges in two dimensions). The displacement and the stress fields inside each element are then retrieved via explicit closed expressions defined element-by-element. The enforcement of the symmetry of the stress tensor via the Voigt notation allows to strongly fulfil the balance of angular momentum and to obtain optimal convergence for both the displacement and stress fields without any reconstruction. Therefore, the solution of the FCFV method does not deteriorate in presence of highly stretched or distorted elements. In addition, it is worth

emphasising that other HDG methods reported in the literature (e.g. [20, 41]), without the Voigt notation proposed in this paper, have shown a sub-optimal rate of convergence in the stress field.

Special attention is given to elastic problems in which classical numerical methods experience volumetric or shear locking. Locking-free finite volume formulations for bending plates [10] have been discussed for both cell-centred and vertex-centred formulations by Wheel [48] and Fallah [17]. Nevertheless, using solid elements, VCFV approaches experience shear locking and additional rotational degrees of freedom are required to handle rigid body motions and accurately predict membrane deformations [34, 46]. In the nearly incompressible limit, the proposed FCFV method is locking-free and the optimal convergence properties are preserved for both the displacement and the stress fields.

The remaining of this paper is organised as follows. In Section 2, the linear elasticity equation using Voigt notation is briefly recalled. The proposed FCFV scheme is presented in Section 3. Section 4 is devoted to the numerical validation of the method in two dimensions. In particular, the optimal orders of convergence are checked for the displacement and stress fields, a sensitivity analysis to the stabilisation parameter and the mesh distortion is performed and the locking-free behaviour is verified for nearly incompressible materials using Kirch's plate and Cook's membrane test cases. In Section 5, several three-dimensional problems involving shear phenomena, pressurised thin shells and complex geometries under realistic loads are discussed to show the capability of the method to handle complex geometries. Finally, Section 6 summarises the conclusions of the work that has been presented.

## 2 Problem statement

Given an open bounded domain  $\Omega \subset \mathbb{R}^{n_{sd}}$ , where  $n_{sd}$  denotes the number of spatial dimensions, the boundary  $\partial\Omega$  is partitioned into the non-overlapping Dirichlet and generalised Neumann boundaries,  $\Gamma_D$  and  $\Gamma_N$  respectively. The behaviour of a deformable solid medium  $\Omega$  is described by

$$\begin{cases} -\nabla \cdot \boldsymbol{\sigma} = \mathbf{f} & \text{in } \Omega, \\ \mathbf{u} = \mathbf{u}_D & \text{on } \Gamma_D, \\ (1 - \xi)\mathbf{P}_n \mathbf{u} + (\mathbf{P}_t + \xi\mathbf{P}_n)\mathbf{n} \cdot \boldsymbol{\sigma} = \xi\mathbf{g}, & \text{on } \Gamma_N, \end{cases} \quad (1)$$

where  $\boldsymbol{\sigma}$  is the Cauchy stress tensor,  $\mathbf{f}$  is the external force,  $\mathbf{u}$  is the displacement field vector,  $\mathbf{n}$  is the outward unit normal vector to  $\Gamma_N$  and the normal and tangent projection matrices are defined as  $\mathbf{P}_n = \mathbf{n} \otimes \mathbf{n}$  and  $\mathbf{P}_t = \mathbf{I}_{n_{sd}} - \mathbf{n} \otimes \mathbf{n}$  respectively. The boundary conditions are given by the imposed displacements on the Dirichlet boundary,  $\mathbf{u}_D$ , and the traction vector on the Neumann boundary,  $\mathbf{g}$ . The parameter  $\xi$  can take a value of one for a pure Neumann boundary or zero for an artificial symmetry boundary, where the normal displacement and the tangential tractions vanish.

**Remark 1.** It is worth noting that a more general boundary condition can be considered to include Dirichlet, Neumann and symmetry boundaries. However, due to the different treatment of Dirichlet boundary conditions in the proposed numerical methodology, the form stated in Equation (1) is preferred in this work.

For a linear elastic material, the well-known Hooke's law provides the relation between stress and strain, namely  $\boldsymbol{\sigma} = \mathbf{C} : \boldsymbol{\varepsilon}(\mathbf{u})$ , where  $\mathbf{C}$  is the fourth order elasticity tensor and the linearised strain tensor is  $\boldsymbol{\varepsilon}(\mathbf{u}) := (\nabla \mathbf{u} + \nabla \mathbf{u}^T) / 2$ .

The so-called Voigt notation [18] is common in this context. The main idea is to exploit the symmetry of the strain and stress tensors. To this end, the strain and stress tensors are reduced to vectors by storing only the non-redundant terms, namely  $\boldsymbol{\varepsilon}_V := [\varepsilon_{11}, \varepsilon_{22}, \gamma_{12}]^T$  and  $\boldsymbol{\sigma}_V := [\sigma_{11}, \sigma_{22}, \tau_{12}]^T$  and  $\boldsymbol{\varepsilon}_V := [\varepsilon_{11}, \varepsilon_{22}, \varepsilon_{33}, \gamma_{12}, \gamma_{13}]^T$  and  $\boldsymbol{\sigma}_V := [\sigma_{11}, \sigma_{22}, \sigma_{33}, \tau_{12}, \tau_{13}, \tau_{23}]^T$  in two and three dimensions respectively, where the number of components of the strain and stress vectors is given by  $m_{sd} = n_{sd}(n_{sd} + 1)/2$ .

Using the Voigt notation, the relation between the displacement and the strain can be written as  $\boldsymbol{\varepsilon}_V = \nabla_S \mathbf{u}$ , where the matrix operator  $\nabla_S \in \mathbb{R}^{m_{sd} \times n_{sd}}$  is given by

$$\nabla_S := \begin{bmatrix} \partial/\partial x_1 & 0 & \partial/\partial x_2 \\ 0 & \partial/\partial x_2 & \partial/\partial x_1 \end{bmatrix}^T \quad (2)$$

and

$$\nabla_S := \begin{bmatrix} \partial/\partial x_1 & 0 & 0 & \partial/\partial x_2 & \partial/\partial x_3 & 0 \\ 0 & \partial/\partial x_2 & 0 & \partial/\partial x_1 & 0 & \partial/\partial x_3 \\ 0 & 0 & \partial/\partial x_3 & 0 & \partial/\partial x_1 & \partial/\partial x_2 \end{bmatrix}^T, \quad (3)$$

in two and three dimensions respectively.

The strain-stress relation given by Hooke's law also simplifies and can be written as  $\boldsymbol{\sigma}_V = \mathbf{D} \boldsymbol{\varepsilon}_V$ , where  $\mathbf{D} \in \mathbb{R}^{m_{sd} \times m_{sd}}$  is a symmetric and positive definite matrix that depends upon the material parameters characterising the medium and, in two dimensions, it also depends upon the model used (i.e. plane strain or plane stress). The matrix  $\mathbf{D}$  is given by

$$\mathbf{D} := \frac{E}{(1 + \nu)(1 - \vartheta\nu)} \begin{bmatrix} 1 + (1 - \vartheta)\nu & \nu & 0 \\ \nu & 1 + (1 - \vartheta)\nu & 0 \\ 0 & 0 & (1 - \vartheta\nu)/2 \end{bmatrix} \quad (4)$$

and

$$\mathbf{D} := \frac{E}{(1 + \nu)(1 - 2\nu)} \begin{bmatrix} 1 - \nu & \nu & \nu & \mathbf{0}_{n_{sd}} \\ \nu & 1 - \nu & \nu & \mathbf{0}_{n_{sd}} \\ \nu & \nu & 1 - \nu & \mathbf{0}_{n_{sd}} \\ \mathbf{0}_{n_{sd}} & \mathbf{0}_{n_{sd}} & \mathbf{0}_{n_{sd}} & (1 - 2\nu)/2 \mathbf{I}_{n_{sd}} \end{bmatrix}, \quad (5)$$

in two and three dimensions respectively, where  $E$  is the Young modulus,  $\nu$  the Poisson ratio. In two dimensions, the parameter  $\vartheta = 1$  denotes a plane stress model whereas  $\vartheta = 2$  denotes a plane strain model.

The strong form of the linear elastic problem can be written using Voigt notation as

$$\begin{cases} -\nabla_{\mathbf{s}}^T \boldsymbol{\sigma}_{\mathbf{v}} = \mathbf{f} & \text{in } \Omega, \\ \mathbf{u} = \mathbf{u}_D & \text{on } \Gamma_D, \\ (1 - \xi)\mathbf{P}_n \mathbf{u} + (\mathbf{P}_t + \xi\mathbf{P}_n)\mathbf{N}^T \boldsymbol{\sigma}_{\mathbf{v}} = \xi \mathbf{g} & \text{on } \Gamma_N, \end{cases} \quad (6)$$

where

$$\mathbf{N} := \begin{bmatrix} n_1 & 0 & n_2 \\ 0 & n_2 & n_1 \end{bmatrix}^T \quad (7)$$

and

$$\mathbf{N} := \begin{bmatrix} n_1 & 0 & 0 & n_2 & n_3 & 0 \\ 0 & n_2 & 0 & n_1 & 0 & n_3 \\ 0 & 0 & n_3 & 0 & n_1 & n_2 \end{bmatrix}^T, \quad (8)$$

in two and three dimensions respectively.

### 3 Face centered finite volume (FCFV) formulation

Let us introduce the *broken computational domain* as a partition of the domain  $\Omega$  in  $\mathbf{n}_{e1}$  disjoint elements  $\Omega_e$  with boundaries  $\partial\Omega_e$ . The set of internal faces  $\Gamma$  is defined as

$$\Gamma := \left[ \bigcup_{e=1}^{\mathbf{n}_{e1}} \partial\Omega_e \right] \setminus \partial\Omega. \quad (9)$$

In addition, the boundary of each element can be written as the union of its faces

$$\partial\Omega_e := \bigcup_{j=1}^{\mathbf{n}_{fa}^e} \Gamma_{e,j}, \quad (10)$$

where  $\mathbf{n}_{fa}^e$  is the total number of faces of the element  $\Omega_e$ .

Following the standard notation using in HDG methods [39], the discrete element spaces

$$\mathcal{V}^h(\Omega) := \{v \in \mathcal{L}_2(\Omega) : v|_{\Omega_e} \in \mathcal{P}^k(\Omega_e) \forall \Omega_e\}, \quad (11a)$$

$$\hat{\mathcal{V}}^h(S) := \{\hat{v} \in \mathcal{L}_2(S) : \hat{v}|_{\Gamma_j} \in \mathcal{P}^k(\Gamma_j) \forall \Gamma_j \subset S \subseteq \Gamma \cup \Gamma_N\}, \quad (11b)$$

are introduced, where  $\mathcal{P}^k(\Omega_e)$  and  $\mathcal{P}^k(\Gamma_j)$  denote the space of polynomials of complete degree at most  $k$  in  $\Omega_e$  and on  $\Gamma_j$  respectively.

### 3.1 Mixed formulation

In the proposed FCFV method, a mixed formulation of the elastic problem of Equation (6) is considered, namely

$$\left\{ \begin{array}{ll} \mathbf{L} + \tilde{\mathbf{D}}\nabla_{\mathbf{s}}\mathbf{u} = \mathbf{0} & \text{in } \Omega_e, \text{ and for } e = 1, \dots, \mathbf{n}_{e1}, \\ \nabla_{\mathbf{s}}^T \tilde{\mathbf{D}}\mathbf{L} = \mathbf{f} & \text{in } \Omega_e, \text{ and for } e = 1, \dots, \mathbf{n}_{e1}, \\ \mathbf{u} = \mathbf{u}_D & \text{on } \Gamma_D, \\ (1 - \xi)\mathbf{P}_n\mathbf{u} - (\mathbf{P}_t + \xi\mathbf{P}_n)\mathbf{N}^T \tilde{\mathbf{D}}\mathbf{L} = \xi\mathbf{g} & \text{on } \Gamma_N, \\ \llbracket \mathbf{u} \otimes \mathbf{n} \rrbracket = \mathbf{0} & \text{on } \Gamma, \\ \llbracket \mathbf{N}^T \tilde{\mathbf{D}}\mathbf{L} \rrbracket = \mathbf{0} & \text{on } \Gamma, \end{array} \right. \quad (12)$$

where the *jump* operator  $\llbracket \cdot \rrbracket$  is defined over an internal face shared by two elements  $\Omega_e$  and  $\Omega_l$  as the sum of the values from the two elements sharing the face [27], namely

$$\llbracket \odot \rrbracket = \odot_e + \odot_l. \quad (13)$$

The matrix  $\tilde{\mathbf{D}}$ , introduced in Equation (12) to guarantee the symmetry of the mixed formulation, is defined as  $\tilde{\mathbf{D}} = \mathbf{V}\mathbf{\Lambda}^{1/2}\mathbf{V}^T$ , after performing the spectral decomposition of the matrix  $\mathbf{D} = \mathbf{V}\mathbf{\Lambda}\mathbf{V}^T$ , where the matrix  $\mathbf{V}$  and the diagonal matrix  $\mathbf{\Lambda}$  contain the eigenvectors and eigenvalues of  $\mathbf{D}$  respectively and  $\mathbf{\Lambda}^{1/2}$  is the diagonal matrix containing the square root of the eigenvalues of  $\mathbf{D}$ .

It is worth noting that the last two equations in (12), called *transmission conditions*, impose the continuity of the displacement field and the normal stress across the internal faces  $\Gamma$ .

### 3.2 FCFV weak formulation

As other HDG methods [8, 9, 28–31, 38, 39], the proposed FCFV method solves the mixed problem in the broken computational domain in two phases. First, a purely Dirichlet problem is defined on each element to write the mixed and primal variables  $(\mathbf{L}_e, \mathbf{u}_e)$  in terms of a new hybrid variable  $\hat{\mathbf{u}}$ , uniquely defined as the trace of the displacement field on  $\Gamma \cup \Gamma_N$ , namely

$$\left\{ \begin{array}{ll} \mathbf{L}_e + \tilde{\mathbf{D}}\nabla_{\mathbf{s}}\mathbf{u}_e = \mathbf{0} & \text{in } \Omega_e \\ \nabla_{\mathbf{s}}^T \tilde{\mathbf{D}}\mathbf{L}_e = \mathbf{f} & \text{in } \Omega_e \\ \mathbf{u}_e = \mathbf{u}_D & \text{on } \partial\Omega_e \cap \Gamma_D, \\ \mathbf{u}_e = \hat{\mathbf{u}} & \text{on } \partial\Omega_e \setminus \Gamma_D, \end{array} \right. \quad (14)$$

for  $e = 1, \dots, \mathbf{n}_{e1}$ . This set of problems are usually referred to as *local problems* and the solution in one element is independent on the solution in the other elements.

Second, the so-called *global problem* is defined to compute the hybrid variable  $\widehat{\mathbf{u}}$ , namely

$$\begin{cases} \llbracket \mathbf{u} \otimes \mathbf{n} \rrbracket = \mathbf{0} & \text{on } \Gamma, \\ \llbracket \mathbf{N}^T \widetilde{\mathbf{D}} \mathbf{L} \rrbracket = \mathbf{0} & \text{on } \Gamma, \\ (1 - \xi) \mathbf{P}_n \mathbf{u} - (\mathbf{P}_t + \xi \mathbf{P}_n) \mathbf{N}^T \widetilde{\mathbf{D}} \mathbf{L} = \xi \mathbf{g} & \text{on } \Gamma_N. \end{cases} \quad (15)$$

It is worth noting that the first transmission condition in Equation (15) is automatically satisfied due to the imposed Dirichlet boundary conditions in the local problems of Equation (14) and the unique definition of the hybrid variable on each face. Therefore, the global problem is simply

$$\begin{cases} \llbracket \mathbf{N}^T \widetilde{\mathbf{D}} \mathbf{L} \rrbracket = \mathbf{0} & \text{on } \Gamma, \\ (1 - \xi) \mathbf{P}_n \mathbf{u} - (\mathbf{P}_t + \xi \mathbf{P}_n) \mathbf{N}^T \widetilde{\mathbf{D}} \mathbf{L} = \xi \mathbf{g} & \text{on } \Gamma_N. \end{cases} \quad (16)$$

Next, the weak formulation of both the local and global problems is presented. For each element  $\Omega_e$ ,  $e = 1, \dots, \mathbf{n}_{e1}$ , the weak formulation of Equation (14) reads as follows: given  $\mathbf{u}_D$  on  $\Gamma_D$  and  $\widehat{\mathbf{u}}$  on  $\Gamma \cup \Gamma_N$ , find  $(\mathbf{L}_e^h, \mathbf{u}_e^h) \in [\mathcal{V}^h(\Omega_e)]^{\text{msd}} \times [\mathcal{V}^h(\Omega_e)]^{\text{nsd}}$  such that

$$-(\mathbf{v}, \mathbf{L}_e^h)_{\Omega_e} + (\nabla_{\mathbf{S}}^T \widetilde{\mathbf{D}} \mathbf{v}, \mathbf{u}_e^h)_{\Omega_e} = \langle \mathbf{N}_e^T \widetilde{\mathbf{D}} \mathbf{v}, \mathbf{u}_D \rangle_{\partial \Omega_e \cap \Gamma_D} + \langle \mathbf{N}_e^T \widetilde{\mathbf{D}} \mathbf{v}, \widehat{\mathbf{u}}^h \rangle_{\partial \Omega_e \setminus \Gamma_D}, \quad (17a)$$

$$-(\nabla_{\mathbf{S}} \mathbf{w}, \widetilde{\mathbf{D}} \mathbf{L}_e^h)_{\Omega_e} + \langle \mathbf{w}, \widehat{\mathbf{N}}_e^T \widetilde{\mathbf{D}} \mathbf{L}_e^h \rangle_{\partial \Omega_e} = (\mathbf{w}, \mathbf{f})_{\Omega_e}, \quad (17b)$$

for all  $(\mathbf{v}, \mathbf{w}) \in [\mathcal{V}^h(\Omega_e)]^{\text{msd}} \times [\mathcal{V}^h(\Omega_e)]^{\text{nsd}}$ .

In the above expressions, the following definition of the internal products of vector functions in  $\mathcal{L}_2(\Omega_e)$  has been used:

$$(\mathbf{p}, \mathbf{q})_{\Omega_e} := \int_{\Omega_e} \mathbf{p} \cdot \mathbf{q} \, d\Omega, \quad \langle \widehat{\mathbf{p}}, \widehat{\mathbf{q}} \rangle_{\partial \Omega_e} := \sum_{j=1}^{\mathbf{n}_{fa}^e} \int_{\Gamma_{e,j}} \widehat{\mathbf{p}} \cdot \widehat{\mathbf{q}} \, d\Gamma. \quad (18)$$

As usual in an HDG context, Dirichlet boundary conditions are imposed in the weak form and the trace of the numerical stress is defined as

$$\widehat{\mathbf{N}}_e^T \widetilde{\mathbf{D}} \mathbf{L}_e^h := \begin{cases} \mathbf{N}_e^T \widetilde{\mathbf{D}} \mathbf{L}_e^h + \boldsymbol{\tau}_e (\mathbf{u}_e^h - \mathbf{u}_D) & \text{on } \partial \Omega_e \cap \Gamma_D, \\ \mathbf{N}_e^T \widetilde{\mathbf{D}} \mathbf{L}_e^h + \boldsymbol{\tau}_e (\mathbf{u}_e^h - \widehat{\mathbf{u}}^h) & \text{elsewhere,} \end{cases} \quad (19)$$

where the stabilisation tensor  $\boldsymbol{\tau}_e$  is introduced to ensure the stability, accuracy and convergence of the resulting numerical scheme [8, 9].

Integrating again by parts Equation (17b) and introducing the definition of Equation (19), the weak formulation of the local problems, for  $e = 1, \dots, \mathbf{n}_{e1}$ , reads: given  $\mathbf{u}_D$  on  $\Gamma_D$  and  $\widehat{\mathbf{u}}$  on  $\Gamma \cup \Gamma_N$ , find  $(\mathbf{L}_e^h, \mathbf{u}_e^h) \in [\mathcal{V}^h(\Omega_e)]^{\text{msd}} \times [\mathcal{V}^h(\Omega_e)]^{\text{nsd}}$  such that

$$-(\mathbf{v}, \mathbf{L}_e^h)_{\Omega_e} + (\nabla_{\mathbf{S}}^T \widetilde{\mathbf{D}} \mathbf{v}, \mathbf{u}_e^h)_{\Omega_e} = \langle \mathbf{N}_e^T \widetilde{\mathbf{D}} \mathbf{v}, \mathbf{u}_D \rangle_{\partial \Omega_e \cap \Gamma_D} + \langle \widehat{\mathbf{N}}_e^T \widetilde{\mathbf{D}} \mathbf{v}, \widehat{\mathbf{u}}^h \rangle_{\partial \Omega_e \setminus \Gamma_D}, \quad (20a)$$

$$(\mathbf{w}, \nabla_{\mathbf{S}}^T \widetilde{\mathbf{D}} \mathbf{L}_e^h)_{\Omega_e} + \langle \mathbf{w}, \boldsymbol{\tau}_e \mathbf{u}_e^h \rangle_{\partial \Omega_e} = (\mathbf{w}, \mathbf{f})_{\Omega_e} + \langle \mathbf{w}, \boldsymbol{\tau}_e \mathbf{u}_D \rangle_{\partial \Omega_e \cap \Gamma_D} + \langle \mathbf{w}, \boldsymbol{\tau}_e \widehat{\mathbf{u}}^h \rangle_{\partial \Omega_e \setminus \Gamma_D}, \quad (20b)$$

for all  $(\mathbf{v}, \mathbf{w}) \in [\mathcal{V}^h(\Omega_e)]^{\text{msd}} \times [\mathcal{V}^h(\Omega_e)]^{\text{nsd}}$ .

Analogously, the weak formulation of the global problem is found by multiplying by a vector of test functions in  $[\hat{\mathcal{V}}^h(\Gamma \cup \Gamma_N)]^{\text{nsd}}$  and adding all the contributions corresponding to internal faces and faces on the Neumann boundary. It reads, find  $\hat{\mathbf{u}}^h \in [\hat{\mathcal{V}}^h(\Gamma \cup \Gamma_N)]^{\text{nsd}}$  that satisfies

$$\begin{aligned} \sum_{e=1}^{\mathbf{n}_{e1}} \left\{ \langle \hat{\mathbf{w}}, \mathbf{N}_e^T \widehat{\mathbf{D}} \mathbf{L}_e^h \rangle_{\partial\Omega_e \setminus \partial\Omega} + \langle \hat{\mathbf{w}}, (1 - \xi) \mathbf{P}_n \hat{\mathbf{u}}^h - (\mathbf{P}_t + \xi \mathbf{P}_n) \mathbf{N}_e^T \widehat{\mathbf{D}} \mathbf{L}_e^h \rangle_{\partial\Omega_e \cap \Gamma_N} \right\} \\ = \sum_{e=1}^{\mathbf{n}_{e1}} \langle \hat{\mathbf{w}}, \xi \mathbf{g} \rangle_{\partial\Omega_e \cap \Gamma_N}, \quad (21) \end{aligned}$$

for all  $\hat{\mathbf{w}} \in [\hat{\mathcal{V}}^h(\Gamma \cup \Gamma_N)]^{\text{nsd}}$ .

By introducing the definition of Equation (19), the weak formulation of the global problem is: find  $\hat{\mathbf{u}}^h \in [\hat{\mathcal{V}}^h(\Gamma \cup \Gamma_N)]^{\text{nsd}}$  such that

$$\begin{aligned} \sum_{e=1}^{\mathbf{n}_{e1}} \left\{ \langle \hat{\mathbf{w}}, \mathbf{N}_e^T \widetilde{\mathbf{D}} \mathbf{L}_e^h \rangle_{\partial\Omega_e \setminus \partial\Omega} + \langle \hat{\mathbf{w}}, \boldsymbol{\tau}_e \mathbf{u}_e^h \rangle_{\partial\Omega_e \setminus \partial\Omega} - \langle \hat{\mathbf{w}}, \boldsymbol{\tau}_e \hat{\mathbf{u}}^h \rangle_{\partial\Omega_e \setminus \partial\Omega} \right. \\ \left. - \langle \hat{\mathbf{w}}, (\mathbf{P}_t + \xi \mathbf{P}_n) \mathbf{N}_e^T \widetilde{\mathbf{D}} \mathbf{L}_e^h \rangle_{\partial\Omega_e \cap \Gamma_N} - \langle \hat{\mathbf{w}}, (\mathbf{P}_t + \xi \mathbf{P}_n) \boldsymbol{\tau}_e \mathbf{u}_e^h \rangle_{\partial\Omega_e \cap \Gamma_N} \right. \\ \left. + \langle \hat{\mathbf{w}}, [(1 - \xi) \mathbf{P}_n + (\mathbf{P}_t + \xi \mathbf{P}_n) \boldsymbol{\tau}_e] \hat{\mathbf{u}}^h \rangle_{\partial\Omega_e \cap \Gamma_N} \right\} = \sum_{e=1}^{\mathbf{n}_{e1}} \langle \hat{\mathbf{w}}, \xi \mathbf{g} \rangle_{\partial\Omega_e \cap \Gamma_N}, \quad (22) \end{aligned}$$

for all  $\hat{\mathbf{w}} \in [\hat{\mathcal{V}}^h(\Gamma \cup \Gamma_N)]^{\text{nsd}}$ .

### 3.3 FCFV spatial discretisation

The proposed FCFV rationale consists of employing a constant degree of approximation within each element for the mixed and primal variables  $\mathbf{L}_e$  and  $\mathbf{u}_e$  and a constant degree of approximation on each face for the hybrid variable  $\hat{\mathbf{u}}$ . The discrete form of the local problem of Equation (20) is obtained as

$$- |\Omega_e| \mathbf{L}_e = \sum_{j \in \mathcal{D}_e} |\Gamma_{e,j}| \widetilde{\mathbf{D}}_j^T \mathbf{N}_j \mathbf{u}_{D,j} + \sum_{j \in \mathcal{B}_e} |\Gamma_{e,j}| \widetilde{\mathbf{D}}_j^T \mathbf{N}_j \hat{\mathbf{u}}_j, \quad (23a)$$

$$\sum_{j \in \mathcal{A}_e} |\Gamma_{e,j}| \boldsymbol{\tau}_j \mathbf{u}_e = |\Omega_e| \mathbf{f}_e + \sum_{j \in \mathcal{D}_e} |\Gamma_{e,j}| \boldsymbol{\tau}_j \mathbf{u}_{D,j} + \sum_{j \in \mathcal{B}_e} |\Gamma_{e,j}| \boldsymbol{\tau}_j \hat{\mathbf{u}}_j, \quad (23b)$$

for  $e = 1, \dots, \mathbf{n}_{e1}$ , where  $\mathbf{L}_e$  and  $\mathbf{u}_e$  denote the constant value of the mixed and primal variables in the element  $\Omega_e$ ,  $\hat{\mathbf{u}}_j$  denotes the constant value of the hybrid variable on the face  $\Gamma_{e,j}$  and the following sets of faces have been introduced for each element:

$$\mathcal{A}_e := \{1, \dots, \mathbf{n}_{\text{fa}}^e\}, \quad \mathcal{D}_e := \{j \in \mathcal{A}_e \mid \Gamma_{e,j} \cap \Gamma_D \neq \emptyset\}, \quad \mathcal{B}_e := \mathcal{A}_e \setminus \mathcal{D}_e, \quad (24)$$



with  $n_{\text{fa}}^e$  the total number of faces of  $\Omega_e$ .

It is worth noting that the discrete form of the local problem has been obtained by utilising a quadrature with one integration point to compute the integrals of the weak formulation.

An important advantage of using of a constant degree of approximation for the mixed and primal variables is that the two equations of the local problem decouple and it is possible to obtain a closed form expression for  $\mathbf{L}_e$  and  $\mathbf{u}_e$  as a function of  $\hat{\mathbf{u}}_j$ , namely

$$\mathbf{L}_e = -|\Omega_e|^{-1}\mathbf{z}_e - |\Omega_e|^{-1} \sum_{j \in \mathcal{B}_e} |\Gamma_{e,j}| \tilde{\mathbf{D}}_j^T \mathbf{N}_j \hat{\mathbf{u}}_j, \quad (25a)$$

$$\mathbf{u}_e = \boldsymbol{\alpha}_e^{-1} \boldsymbol{\beta}_e + \boldsymbol{\alpha}_e^{-1} \sum_{j \in \mathcal{B}_e} |\Gamma_{e,j}| \boldsymbol{\tau}_j \hat{\mathbf{u}}_j, \quad (25b)$$

where

$$\begin{aligned} \boldsymbol{\alpha}_e &:= \sum_{j \in \mathcal{A}_e} |\Gamma_{e,j}| \boldsymbol{\tau}_j, & \boldsymbol{\beta}_e &:= |\Omega_e| \mathbf{f}_e + \sum_{j \in \mathcal{D}_e} |\Gamma_{e,j}| \boldsymbol{\tau}_j \mathbf{u}_{D,j}, \\ \mathbf{z}_e &:= \sum_{j \in \mathcal{D}_e} |\Gamma_{e,j}| \tilde{\mathbf{D}}_j^T \mathbf{N}_j \mathbf{u}_{D,j}. \end{aligned} \quad (26)$$

Similarly, employing a constant degree of approximation for  $\mathbf{L}_e$ ,  $\mathbf{u}_e$  and  $\hat{\mathbf{u}}$ , the discrete form of the global problem of Equation (22) is

$$\sum_{e=1}^{n_{e1}} |\Gamma_{e,i}| \left\{ \mathbf{A}_{e,i} \mathbf{N}_i^T \tilde{\mathbf{D}}_i \mathbf{L}_e + \mathbf{A}_{e,i} \boldsymbol{\tau}_i \mathbf{u}_e + \mathbf{B}_{e,i} \hat{\mathbf{u}}_i \right\} = \xi \sum_{e=1}^{n_{e1}} |\Gamma_{e,i}| \mathbf{g}_i \chi_{\mathcal{N}_e}(i), \quad (27)$$

for  $i \in \mathcal{B}_e$ , where  $\chi_{\mathcal{I}_e}$  and  $\chi_{\mathcal{N}_e}$  are the indicator functions of the sets  $\mathcal{I}_e := \{j \in \mathcal{A}_e \mid \Gamma_{e,j} \cap \partial\Omega = \emptyset\}$  and  $\mathcal{N}_e := \{j \in \mathcal{A}_e \mid \Gamma_{e,j} \cap \Gamma_N \neq \emptyset\}$  respectively. The following matrices have been introduced to shorten the notation in Equation (27)

$$\mathbf{A}_{e,i} = \mathbf{I}_{\text{nsd}} \chi_{\mathcal{I}_e}(i) - (\mathbf{P}_t + \xi \mathbf{P}_n) \chi_{\mathcal{N}_e}(i), \quad (28a)$$

$$\mathbf{B}_{e,i} = -\boldsymbol{\tau}_i \chi_{\mathcal{I}_e}(i) + [(1 - \xi) \mathbf{P}_n + (\mathbf{P}_t + \xi \mathbf{P}_n) \boldsymbol{\tau}_i] \chi_{\mathcal{N}_e}(i). \quad (28b)$$

After introducing the closed form expressions of the mixed and primal variable of Equation (25) in Equation (27), a linear system of equations is obtained, where the only unknown is the hybrid variable defined over the interior and Neumann faces,  $\Gamma \cup \Gamma_N$ , namely

$$\widehat{\mathbf{K}} \hat{\mathbf{u}} = \hat{\mathbf{f}}. \quad (29)$$

The matrix  $\widehat{\mathbf{K}}$  and the vector  $\hat{\mathbf{f}}$  are obtained by assembling the elemental contributions

$$\widehat{\mathbf{K}}_{i,j}^e := |\Gamma_{e,i}| \left\{ |\Gamma_{e,j}| \mathbf{A}_{e,i} (\boldsymbol{\tau}_i \boldsymbol{\alpha}_e^{-1} \boldsymbol{\tau}_j - |\Omega_e|^{-1} \mathbf{N}_i^T \tilde{\mathbf{D}}_i \tilde{\mathbf{D}}_j^T \mathbf{N}_j) + \mathbf{B}_{e,i} \delta_{ij} \right\}, \quad (30a)$$

$$\hat{\mathbf{f}}_i^e := |\Gamma_{e,i}| \left\{ -\mathbf{A}_{e,i} (\boldsymbol{\tau}_i \boldsymbol{\alpha}_e^{-1} \boldsymbol{\beta}_e - |\Omega_e|^{-1} \mathbf{N}_i^T \tilde{\mathbf{D}}_i \mathbf{z}_e) + \xi \mathbf{g}_i \chi_{\mathcal{N}_e}(i) \right\}, \quad (30b)$$

for  $i, j \in \mathcal{B}_e$  and  $\delta_{ij}$  being the classical Kronecker delta, equal to 1 if  $i = j$  and 0 otherwise.

## 4 Two dimensional examples

This Section presents three numerical examples in two dimensions. The first example is used in order to validate the optimal rate of convergence, to illustrate the robustness of the proposed FCFV approach in the incompressible limit, to numerically study the effect of the stabilisation parameter and to demonstrate the robustness in terms of element distortion. The last two examples involve classical test cases for linear elastic solvers, namely the Kirsch's plate and the Cook's membrane problems.

### 4.1 Optimal order of convergence

The first example considers a mesh convergence study to verify the optimal approximation properties of the proposed FCFV method in two dimensions. The model problem of Equation (1), defined in  $\Omega = [0, 1]^2$ , is considered. The external force and boundary conditions are selected so that the exact solution [41] is given by

$$u_1(x_1, x_2) = -x_1^2 x_2 (x_1 - 1)^2 (x_2 - 1) (2x_2 - 1), \quad (31a)$$

$$u_2(x_1, x_2) = x_2^2 x_1 (x_2 - 1)^2 (x_1 - 1) (2x_1 - 1). \quad (31b)$$

The traction corresponding to the analytical solution is imposed on  $\Gamma_N = \{(x_1, x_2) \in \mathbb{R}^2 \mid x_2 = 0\}$ , whereas homogeneous Dirichlet boundary conditions are imposed on the rest of the boundary.

Structured uniform quadrilateral meshes with characteristic element size  $h = 2^{-r}$  are generated, where  $r$  denotes the level of mesh refinement. Triangular uniform meshes are obtained by subdivision of each quadrilateral in four triangles using the two diagonals of the quadrilateral.

The computed Von Mises stress on three quadrilateral meshes is represented in Figure 1, illustrating the increasing accuracy offered by the proposed FCFV as the mesh is refined.

Figure 2 displays the error of the computed displacement and the stress fields in the  $\mathcal{L}_2(\Omega)$  norm as a function of the characteristic element size for both quadrilateral and triangular meshes on a medium with  $E = 1$  and  $\nu = 1/3$ . It can be observed that the error converges with the expected rate of convergence for both the displacement and the stress. It is important to emphasise that the proposed FCFV produces a stress field with an error that converges linearly to the exact solution without performing a reconstruction of the displacement field. In addition, the proposed approach provides similar accuracy for both the displacement and the stress field due to the use of a mixed formulation.

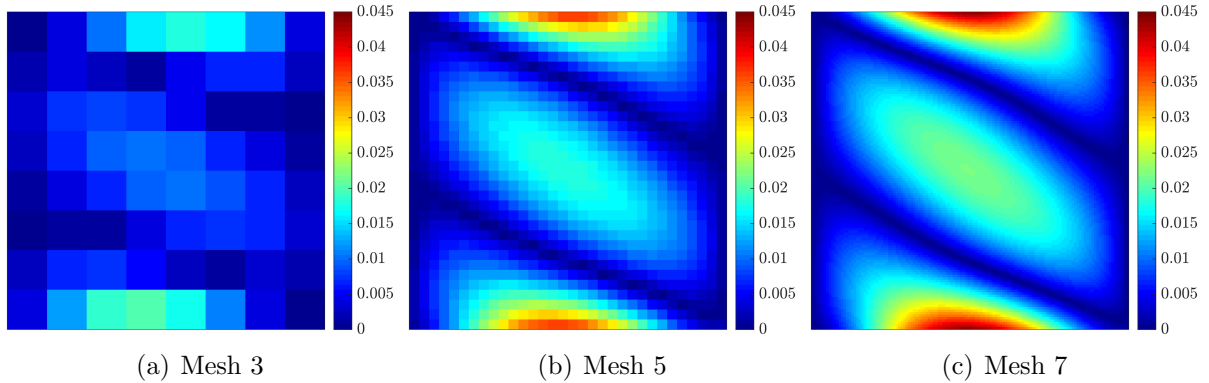


Figure 1: Von Mises stress on three quadrilateral meshes.

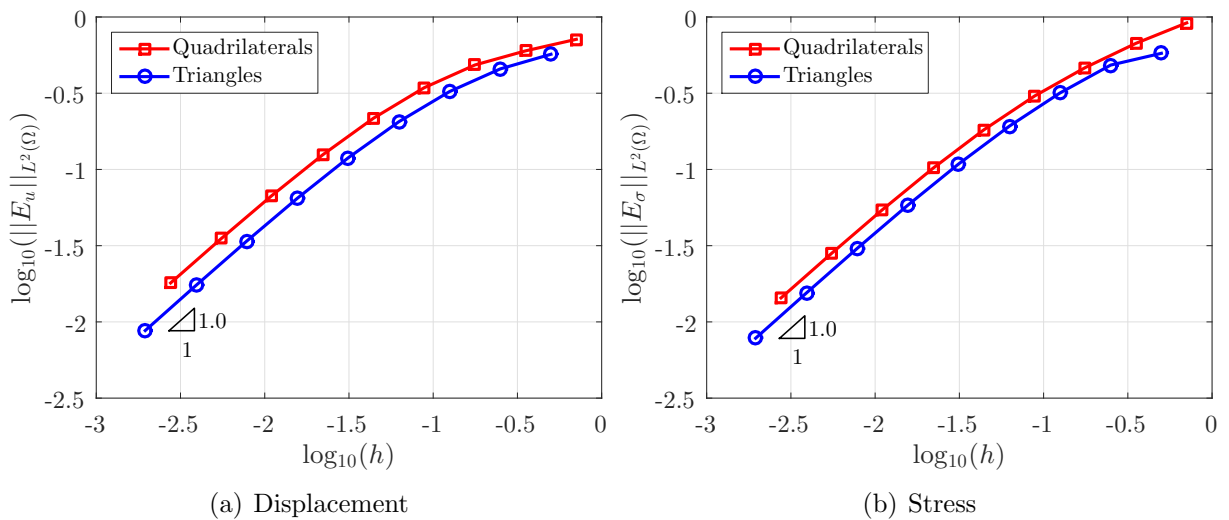


Figure 2: Mesh convergence of the  $\mathcal{L}_2(\Omega)$  error of the (a) displacement and (b) the stress, for quadrilateral and triangular elements in a medium with  $\nu = 1/3$ .

## 4.2 Locking-free behaviour for nearly incompressible materials

To demonstrate the robustness of the proposed approach for nearly incompressible materials, the problem considered in Section 4.1 is studied for a material with  $E = 1$  and  $\nu = 0.49999$ . Figure 3 displays the error of the computed displacement and the stress fields in the  $\mathcal{L}_2(\Omega)$  norm as a function of the characteristic element size for both quadrilateral and triangular meshes. The results exhibit the optimal order of convergence for both the displacement and the stress. In addition, by comparing Figures 3 and 2 it can be observed that almost identical results are obtained irrespectively of the value of the Poisson ratio, illustrating the robustness and suitability of the proposed approach for nearly incompressible materials.

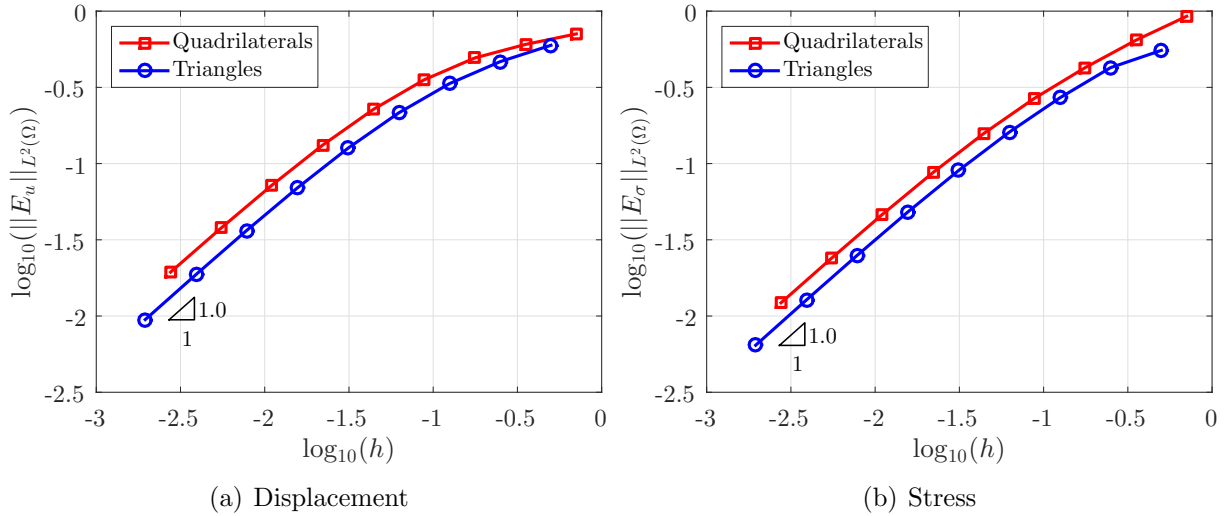


Figure 3: Mesh convergence of the  $\mathcal{L}_2(\Omega)$  error of the (a) displacement and (b) the stress, for quadrilateral and triangular elements in a medium with  $\nu = 0.49999$ .

### 4.3 Optimal value of the stabilisation parameter

The proposed methodology requires the choice of the stabilisation tensor  $\boldsymbol{\tau}$ . Previous works by Cockburn and co-workers [8, 9, 41] have shown that the stabilisation can have a sizeable effect on the accuracy, convergence and stability of the HDG method. To illustrate the effect of this parameter, the stabilisation tensor is selected as  $\boldsymbol{\tau} = \tau(E/\ell)\mathbf{I}_{\text{nsd}}$ , where  $\ell$  is a characteristic length. The evolution of the error of the displacement and the stress in the  $\mathcal{L}_2(\Omega)$  norm as a function of the stabilisation parameter  $\tau$  is represented in Figure 4 for two different computational meshes and for both quadrilateral and triangular elements. It can be observed that there is an optimum value of the stabilisation parameter, approximately  $\tau = 3$ . It is worth noting that the optimum value is independent on the discretisation considered as the same value provides the most accurate results for all levels of mesh refinement and for all types of element. In addition, the value obtained here for the linear elastic problem also coincides with the optimal value reported in [36] for the solution of heat transfer problems.

### 4.4 Influence of the mesh distortion

Traditional finite volume methods (e.g. cell-centred and vertex-centred) are well known to suffer an important loss of accuracy when the mesh contains highly distorted elements [12–15]. The accuracy of the reconstruction of the displacement field, required to produce an accurate stress field, is severely compromised by the presence of low quality elements.

To illustrate the robustness of the FCFV method in highly distorted meshes, a new set of meshes is produced by introducing a perturbation of the interior nodes of the uniform

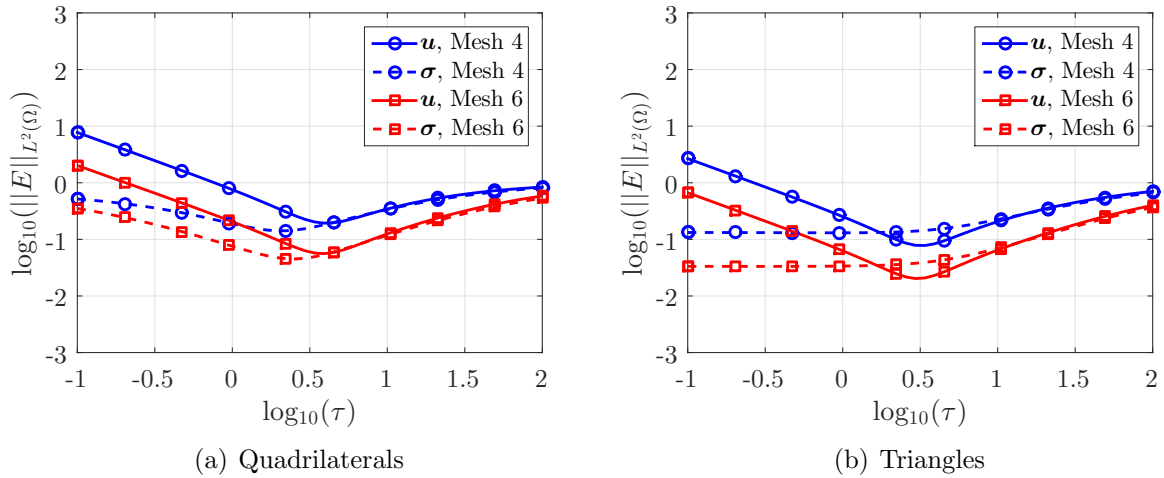


Figure 4: Error of the displacement and the stress in the  $\mathcal{L}_2(\Omega)$  norm as a function of the stabilisation parameter  $\tau$ .

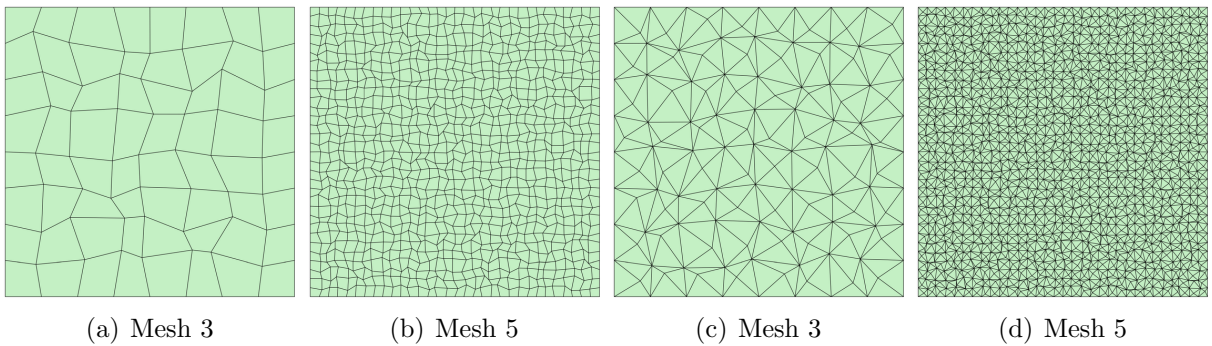


Figure 5: Distorted quadrilateral and triangular meshes of the domain  $\Omega = [0, 1]^2$ .

meshes employed in the previous example. The new position of an interior node is computed as  $\tilde{\mathbf{x}}_i = \mathbf{x}_i + \mathbf{r}_i$ , where  $\mathbf{x}_i$  denotes the position in the original uniform mesh and  $\mathbf{r}_i \in \mathbb{R}^{n_{sd}}$  is a vector containing random numbers generated within the interval  $[-h_{\min}/3, h_{\min}/3]$ , with  $h_{\min}$  being the minimum edge length of the uniform mesh. Two of the meshes with highly distorted elements produced with this strategy are shown in Figure 5, for both quadrilateral and triangular elements.

The numerical experiment of Section 4.2 (i.e. for a nearly incompressible medium) is repeated using the distorted quadrilateral and triangular meshes. Figure 6 shows the error of the computed displacement and stress fields in the  $\mathcal{L}_2(\Omega)$  norm as a function of the characteristic element size, computed as the maximum of the element diameters in the mesh. The results show the expected optimal rate of convergence for both the displacement and the stress, clearly demonstrating that the convergence properties of the proposed approach do not depend upon the quality of the mesh. In addition, by comparing

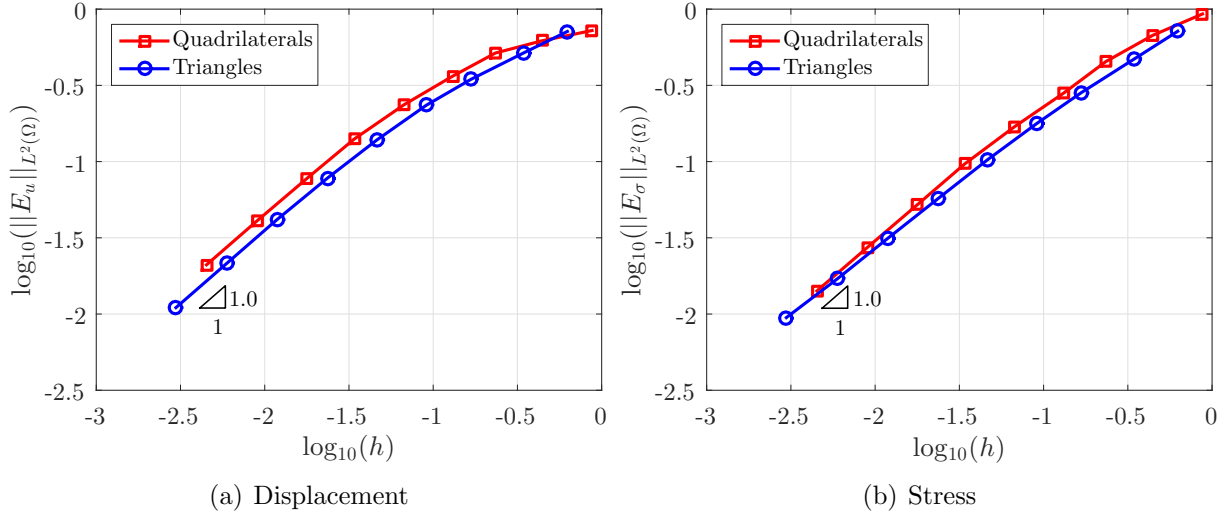


Figure 6: Mesh convergence of the  $\mathcal{L}_2(\Omega)$  error of the (a) displacement and (b) the stress, for highly distorted quadrilateral and triangular elements in a medium with  $\nu = 0.49999$ .

the results of Figures 6 and 3, it can be concluded that the large distortion introduced in the mesh does not result in a sizeable loss of accuracy. For instance, the  $\mathcal{L}_2(\Omega)$  error of the displacement on the uniform mesh of triangular elements in the three finest meshes is 0.037, 0.019 and 0.010 respectively, whereas the error on the corresponding distorted meshes is 0.042, 0.022 and 0.011 respectively.

## 4.5 Kirch's plate problem

The next example considers the computation of the stress field in an infinite plate with a circular hole subject to a uniform tension of magnitude  $\sigma_0$  in the horizontal direction, a classical test case for solid mechanics solvers in two dimensions [43, 44]. The exact solution of the problem is given in polar coordinates by

$$u_1(r, \theta) = \frac{\sigma_0 a}{8\mu} \left\{ (k+1) \frac{r}{a} \left( 1 + \frac{2a^2}{r^2} \right) \cos(\theta) + \frac{2a}{r} \left( 1 - \frac{a^2}{r^2} \right) \cos(3\theta) \right\} \quad (32a)$$

$$u_2(r, \theta) = \frac{\sigma_0 a}{8\mu} \left\{ \frac{r}{a} \left( (k-3) - (k-1) \frac{2a^2}{r^2} \right) \sin(\theta) + \frac{2a}{r} \left( 1 - \frac{a^2}{r^2} \right) \sin(3\theta) \right\} \quad (32b)$$

where  $\mu$  is the shear modulus and the Kolosov's constant is defined as  $k = (3 - \nu)/(1 + \nu)$  for plane stress and  $k = 3 - 4\nu$  for plane strain.

The finite computational domain is selected as  $[-L, L]^2 \setminus \mathcal{D}_{0,a}$ , where  $\mathcal{D}_{0,a}$  denotes the disk of radius  $a$  centred at the origin. Using the symmetry of the problem, only a quarter of the domain is considered, as illustrated in Figure 7.

For the numerical examples,  $L = 4\text{m}$ ,  $a = 1\text{m}$ ,  $E = 10^5\text{Pa}$ ,  $\nu = 0.3$  and  $\sigma_0 = 10\text{Pa}$

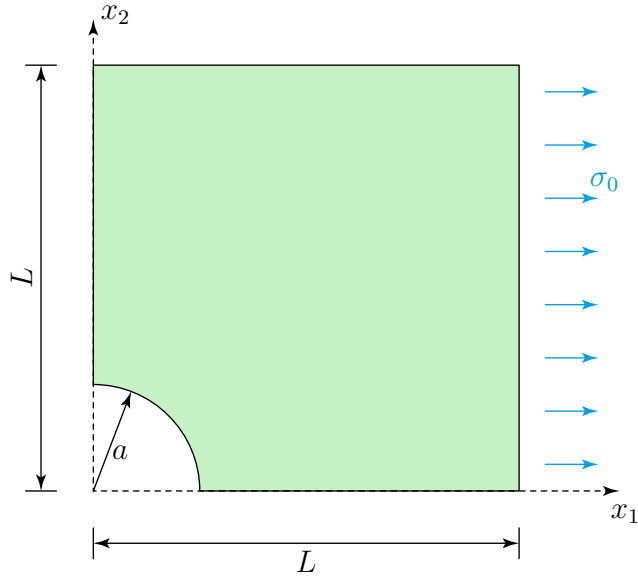


Figure 7: Computational domain for the Kirch's plate problem.

are considered. To avoid any effect from the truncation of the infinite domain, the exact traction is imposed on the right and top boundaries, zero traction is imposed on the circular boundary and symmetry boundary conditions are imposed on the bottom and left boundaries.

The convergence of the displacement and stress error measured in the  $\mathcal{L}_2(\Omega)$  norm as a function of the characteristic element size is shown in Figure 8, showing the expected rate for both quantities.

The stress field computed on the seventh mesh used for the mesh convergence study, with 573,123 triangular elements, is shown in Figure 9. The computation with the proposed FCFV method required the solution of a linear system of 1,719,826 equations, taking 6 seconds to compute all elemental matrices, 3 seconds to perform the assembly of the global system and 46 seconds to solve using a direct method. The developed code is written in Matlab and the computation was performed in an Intel<sup>®</sup> Xeon<sup>®</sup> CPU @ 3.70GHz and 32GB main memory available.

## 4.6 Cook's membrane problem

The last two dimensional example considers a classical bending dominated test case employed to validate the susceptibility of linear elastic solvers to volumetric locking, the so-called Cook's membrane problem [10]. The problem consists of a tapered plate clamped on one end and subject to a shear load, taken as  $\mathbf{g} = (0, 1/16)$  here, on the opposite end, as illustrated in Figure 10.

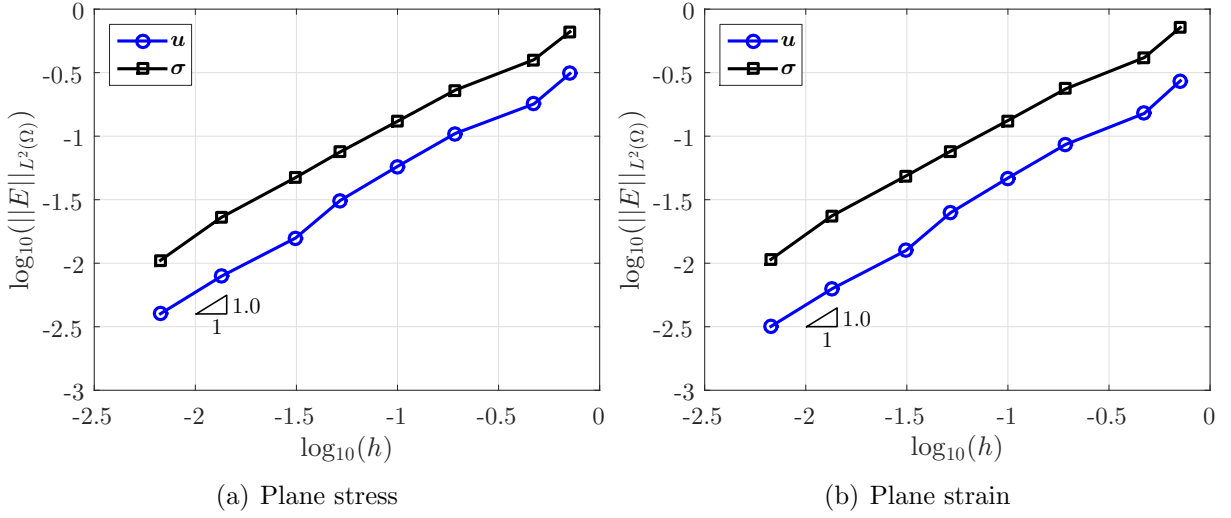


Figure 8: Kirch's plate problem: mesh convergence of the  $\mathcal{L}_2(\Omega)$  error of the displacement and the stress for a (a) plane stress and (b) plane strain two dimensional models.

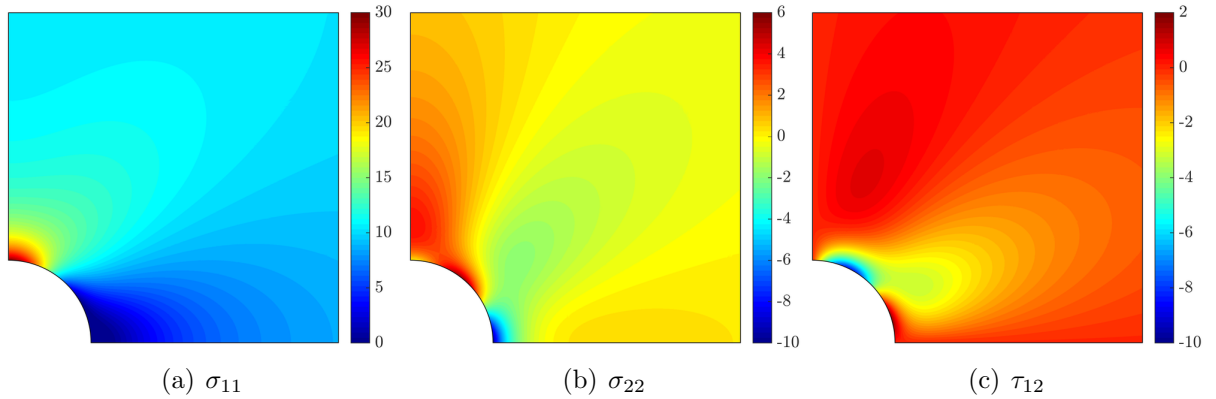


Figure 9: Kirch's plate problem: computed components of the stress field.

Two cases, reported in [1], are considered to validate the performance of the recently proposed FCFV methodology. The first case involves a material with Young modulus  $E = 1$  and Poisson ratio  $\nu = 1/3$  and the second case a nearly incompressible material with Young modulus  $E = 1.12499998125$  and Poisson ratio  $\nu = 0.499999975$ . As there is no analytical solution available, the vertical displacement at the mid point of the right end of the plate,  $\mathbf{Q} = (48, 52)$ , is compared against the reference values reported in [1], given by 21.520 and 16.442 respectively.

Figure 11 shows the convergence of the vertical displacement at point  $\mathbf{Q}$  for both cases and using both quadrilateral and triangular elements. The results indicate convergence of the vertical displacement in the ninth mesh, with 262,144 elements, for the first case with  $\nu = 1/3$ . The computed displacement at the mid point of the right end of the plate is



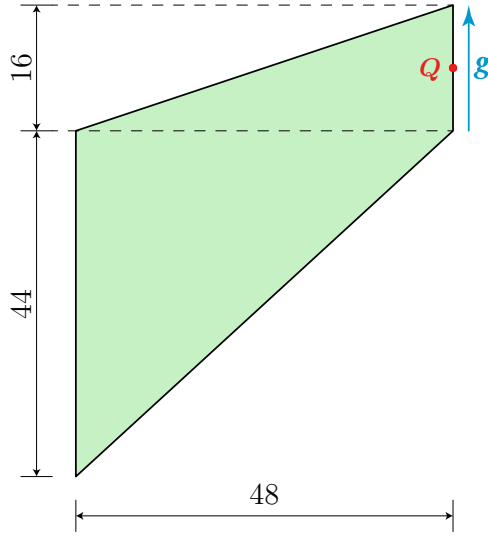


Figure 10: Cook's membrane problem.

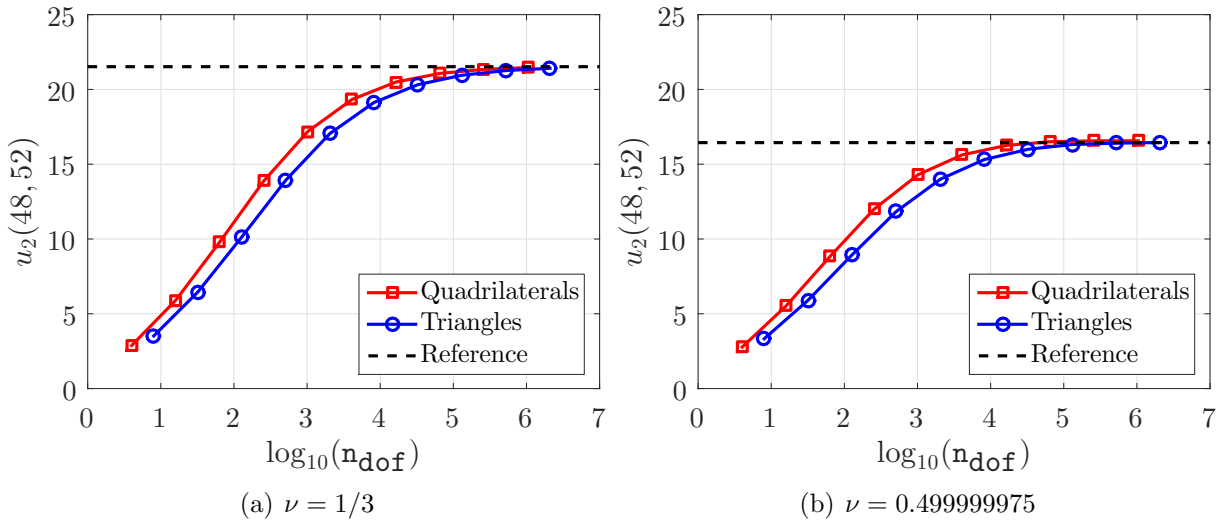


Figure 11: Cook's membrane problem: evolution of the vertical displacement at the midpoint of the right end of the plate as a function of the total number of degrees of freedom.

within a 1% difference with respect to the results reported in [1]. The FCFV computation required the solution of a linear system of 1,049,600 equations, taking 4 seconds to compute all elemental matrices, 2 seconds to perform the assembly of the global system and 1 minute to solve using a direct method. The displacement field and Von Mises stress for this computation are represented in Figure 12.

For the second case, with a nearly incompressible material, the results in the eight mesh, with 65,536 elements, show convergence to the reference value, illustrating the robustness

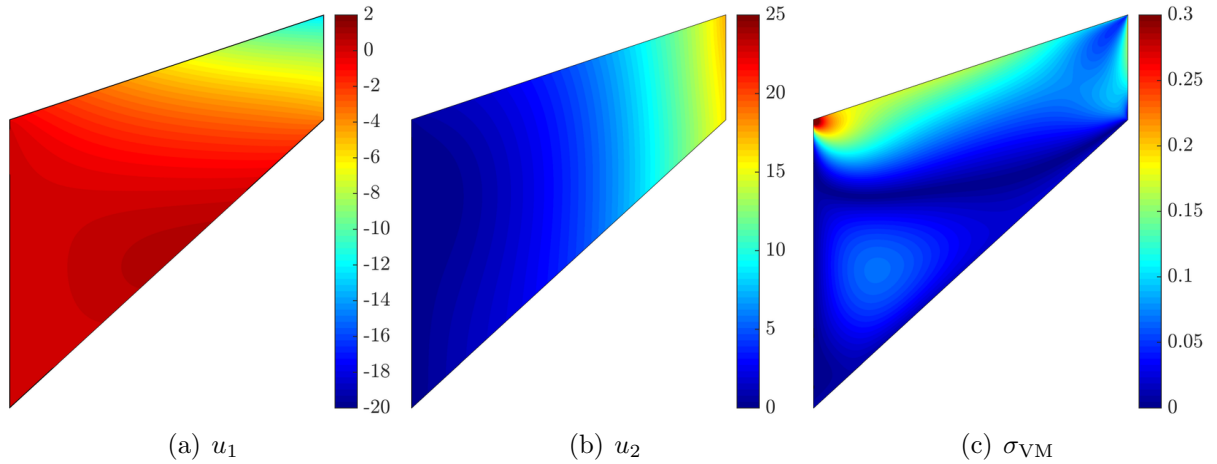


Figure 12: Cook's membrane problem: displacement and Von Mises stress.

and accuracy of the proposed approach in the incompressible limit. The computed displacement at the mid point of the right end of the plate is within a 0.5% difference with respect to the results reported in [1]. The FCFV computation required the solution of a linear system of 262,656 equations, taking 1 second to compute all elemental matrices, 0.5 seconds to perform the assembly of the global system and 10 seconds to solve using a direct method.

## 5 Three dimensional examples

This Section presents three numerical examples in three dimensions to show the potential of the proposed FCFV approach in more complicated scenarios, including a more realistic application involving a complex geometry.

### 5.1 Cantilever beam under shear

The first three-dimensional example involves the analysis of a beam under shear and it is used here to verify the optimal convergence properties of the FCFV method in three dimensions for both hexahedral and tetrahedral elements.

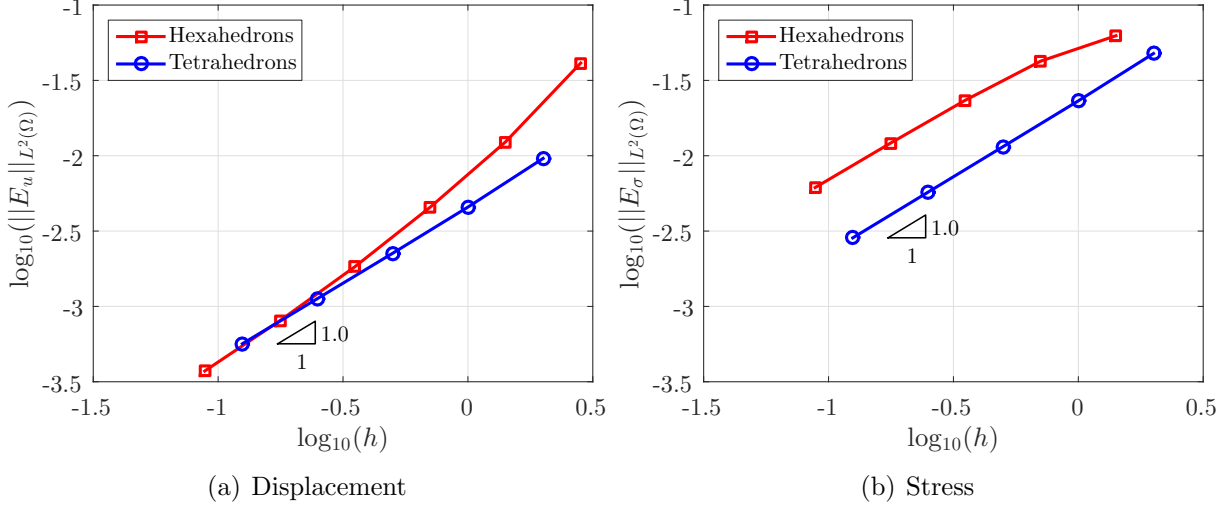


Figure 13: Cantilever beam under shear: mesh convergence of the  $\mathcal{L}_2(\Omega)$  error of the (a) displacement and (b) the stress, for hexahedral and tetrahedral elements.

The analytical solution of the problem is given by [3]

$$u_1(x_1, x_2, x_3) = \frac{3P\nu}{4E} x_1 x_2 x_3, \quad (33a)$$

$$u_2(x_1, x_2, x_3) = \frac{P}{8E} [3\nu x_3 (x_1^2 - x_2^2) - x_3^3], \quad (33b)$$

$$u_3(x_1, x_2, x_3) = \frac{Px_2}{8E} [\nu(3x_1^2 - x_2^2 + 4) + 3x_3^2 - 2x_2^2 + 6] - \frac{3P\nu}{\pi^3 E} \sum_{n=1}^{\infty} \frac{(-1)^n}{n^3 \cosh(n\pi)} \cos(n\pi x) \sinh(n\pi y). \quad (33c)$$

The domain is  $\Omega = [-1, 1] \times [-1, 1] \times [0, L]$  and the material properties are taken as  $E = 25$  and  $\nu = 0.3$ . Following [21], the boundary conditions correspond to the exact displacement imposed on  $\Gamma_D = \{(x_1, x_2, x_3) \in \mathbb{R}^3 \mid x_3 = L\}$  whereas the exact tractions are imposed at  $\Gamma_N = \partial\Omega \setminus \Gamma_D$ . The length of beam is  $L = 10$  and the shear load is taken as  $P = 0.1$ .

Five tetrahedral and six hexahedral meshes are considered to perform the mesh convergence analysis. The tetrahedral meshes contain 120, 960, 7,680, 61,440 and 491,520 elements respectively, whereas the hexahedral meshes contain 5, 40, 320, 2,560, 20,480 and 163,840 elements respectively. Figure 13 displays the error of the computed displacement and the stress fields in the  $\mathcal{L}_2(\Omega)$  norm as a function of the characteristic element size, showing the optimal approximation properties of the proposed FCFV method in three dimensions for both hexahedral and tetrahedral elements.

The three components of the displacement and the Von Mises stress are represented in Figure 14. The results, corresponding to the finer tetrahedral mesh are displayed over the

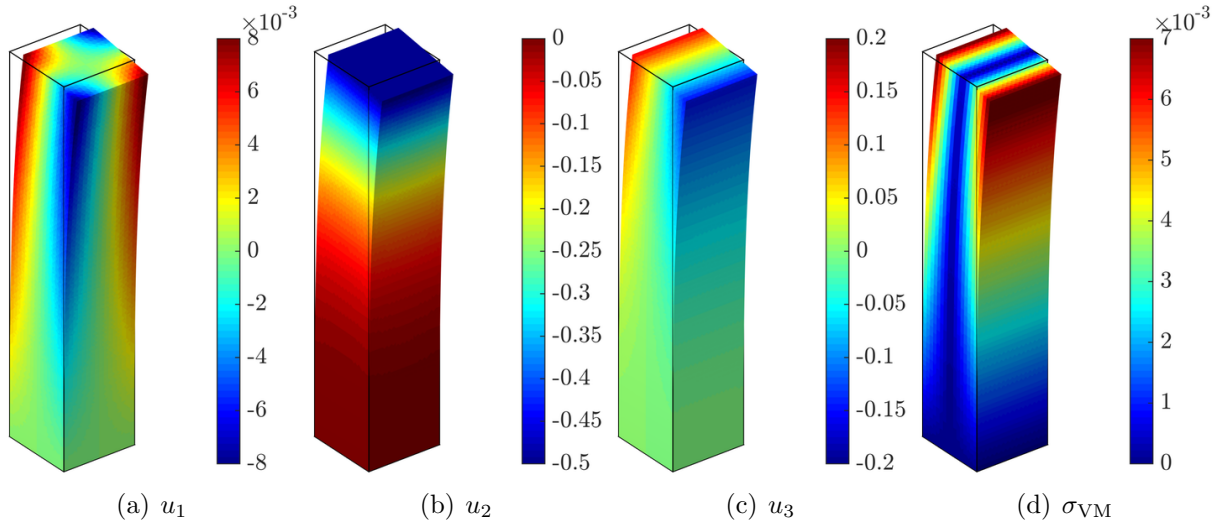


Figure 14: Cantilever beam under shear: displacement and Von Mises stress.

deformed configuration. The computation with the proposed FCFV method required the solution of a linear system of 2,915,328 equations, taking 10 seconds to compute all elemental matrices, 5 seconds to perform the assembly of the global system and 10 minutes to solve using a direct method. The developed code is written in Matlab and the computation was performed in an Intel® Xeon® CPU @ 3.70GHz and 32GB main memory available.

## 5.2 Thin cylindrical shell

The next example involves the analysis of a thin cylindrical shell subject to a uniform internal pressure and with fixed ends. This is a particularly challenging problem for low order methods due to the localised bending occurring near the ends of the shell, leading to a radial displacement that exhibits a boundary layer behaviour.

The analytical solution of the problem is given by [45]

$$u_1(x_1, x_2, x_3) = u_r(x_3), \cos(\theta) \quad (34a)$$

$$u_2(x_1, x_2, x_3) = u_r(x_3), \sin(\theta) \quad (34b)$$

$$u_3(x_1, x_2, x_3) = 0, \quad (34c)$$

where  $u_r$  denotes the radial displacement, given by

$$u_r(x_3) = -\frac{Pa^2}{Et} (1 - C_1 \sin(\beta x_3) \sinh(\beta x_3) - C_2 \cos(\beta x_3) \cosh(\beta x_3)), \quad (35)$$

with

$$C_1 = \frac{2 \sin(\alpha) \sinh(\alpha)}{\cos(2\alpha) + \cosh(2\alpha)}, \quad C_2 = \frac{2 \cos(\alpha) \cosh(\alpha)}{\cos(2\alpha) + \cosh(2\alpha)}. \quad (36)$$

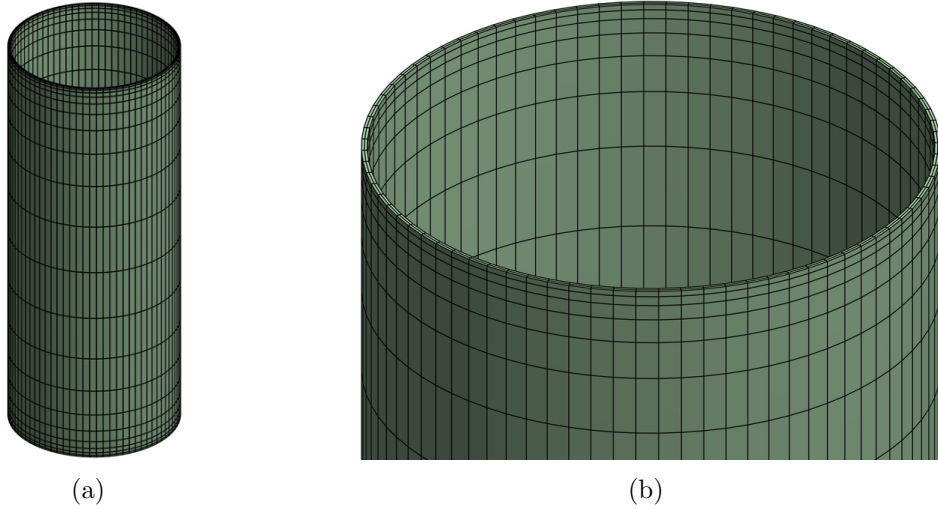


Figure 15: Thin cylindrical shell: (a) hexahedral mesh with element stretching near the ends of the shell and (b) detail of the mesh showing the two elements across the thickness.

In the above expressions,  $P$  is the magnitude of the internal pressure,  $a$  is the midplane radius of the shell,  $t$  is the thickness,

$$\alpha = \frac{\beta L}{2}, \quad \beta = \left( \frac{Et}{4a^2 D} \right)^{1/4}, \quad D = \frac{Et^3}{12(1 - \nu^3)} \quad (37)$$

and  $L$  is the height of the shell.

The numerical results presented here consider  $L = 5$ ,  $a = 1$ ,  $t = 0.02$ ,  $E = 1$  and  $\nu = 0.3$ . Hexahedral meshes with element stretching are considered to capture the localised variation of the displacement near the ends of the shell. Figure 15 shows one hexahedral mesh with 3,200 elements and a detail of the mesh near the end, illustrating the stretching used and showing that only two elements are considered across the thickness. It is worth emphasising that the problem is solved using solid elements despite the shell theory is applicable in this problem [45].

The three components of the displacement field and the radial displacement are depicted in Figure 16 on a fine mesh with 819,200 elements. The results are in excellent agreement with the shell theory, with an  $\mathcal{L}_2(\Omega)$  error of  $9.1 \times 10^{-4}$  and  $4.1 \times 10^{-3}$  in the displacement and stress respectively.

Figure 17 shows a detailed view of the radial displacement computed with five subsequently refined meshes and compared to the analytical solution. The results show the ability of the proposed FCFV methodology to capture the boundary layer behaviour of the radial displacement with a mesh with only two elements across the thickness.

A more quantitative analysis is presented in Table 1, where the number of elements the number of degrees of freedom and the error of the displacement field, the stress field

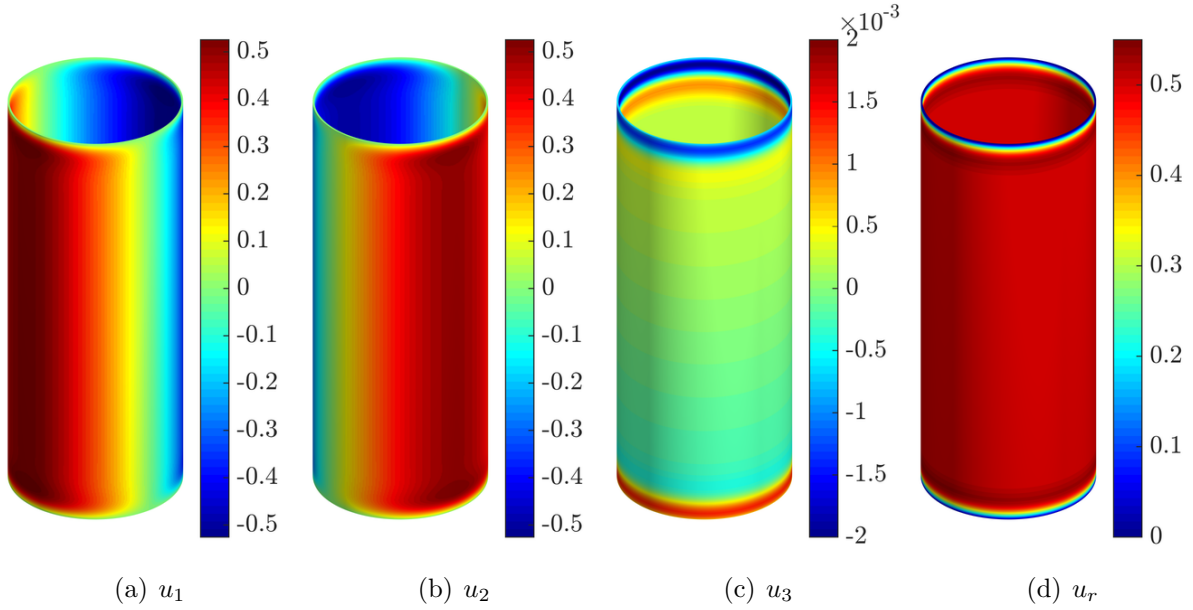


Figure 16: Thin cylindrical shell: components of the displacement field and radial displacement.

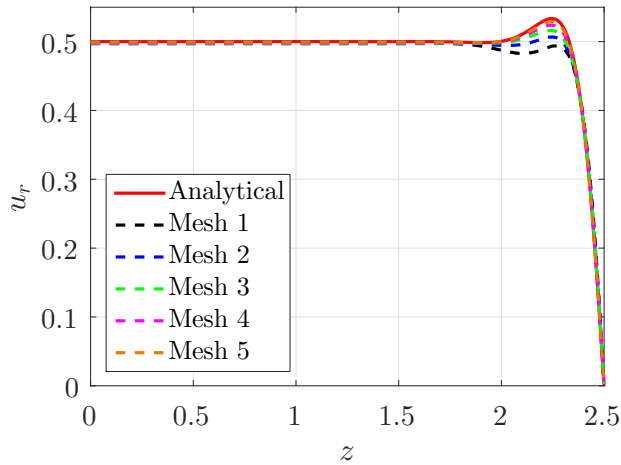


Figure 17: Thin cylindrical shell: mesh convergence of the radial displacement.

and the radial displacement is given for the five meshes utilised. The error of the radial displacement is measured over a section, corresponding to  $x_1 = x_1^*$  and  $x_2 = x_2^*$ , as

$$E_r = \left\{ \frac{\int_{-L/2}^{L/2} [u_r^h(x_1^*, x_2^*, x_3) - u_r(x_3)]^2 dx_3}{\int_{-L/2}^{L/2} u_r(x_3)^2 dx_3} \right\}^{1/2}, \quad (38)$$

where  $u_r^h$  and  $u_r$  are the computed and exact radial displacement respectively.

Mesh	Elements	$n_{\text{dof}}$	$E_u$	$E_\sigma$	$E_r$
1	$80 \times 10 \times 2$	33,480	0.0055	0.0764	0.0285
2	$160 \times 20 \times 2$	134,160	0.0035	0.0409	0.0191
3	$320 \times 40 \times 2$	997,440	0.0021	0.0224	0.0124
4	$640 \times 80 \times 2$	3,991,680	0.0011	0.0116	0.0070
5	$1280 \times 160 \times 2$	8,599,680	0.0005	0.0055	0.0031

Table 1: Thin cylindrical shell: details of the mesh convergence analysis. For each mesh, the number of elements, the number of degrees of freedom and the error of the displacement field, the stress field and the radial displacement are given.

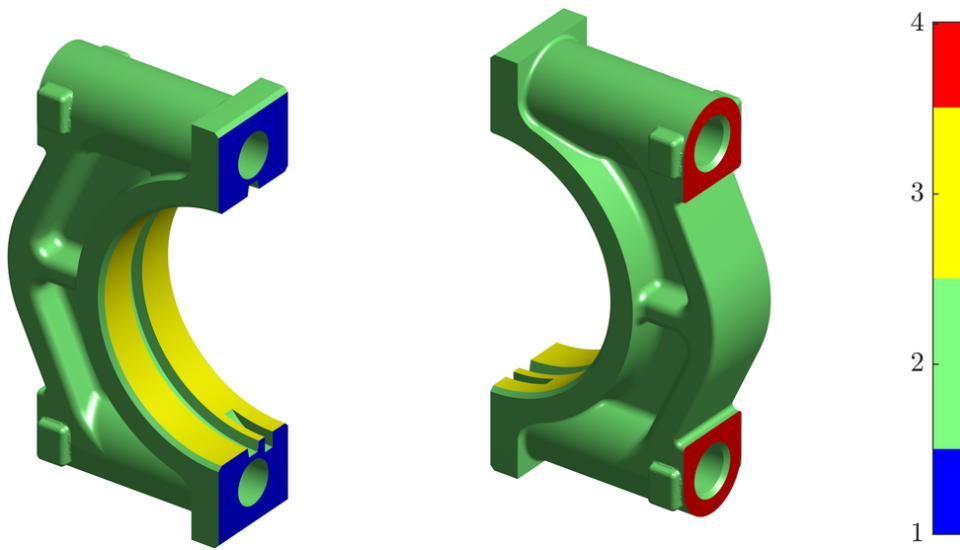


Figure 18: Bearing cap: geometric model with the colours representing the different boundary conditions.

The results in Table 1 show, once more, the optimal first-order convergence of the error of the displacement and stress fields under mesh refinement.

### 5.3 Bearing cap

The last example considers the application of the proposed FCFV approach in a realistic setting involving the stress analysis of a bearing cap used in the automotive industry. Figure 18 shows the geometry of the component, where the different colours represent the different boundary conditions. A homogeneous Dirichlet boundary condition is applied to the surfaces in blue, where the bearing cap is fixed. Neumann boundary conditions, enforcing a prescribed pressure of  $P = 130\text{N/mm}^2$ , are imposed on the surfaces in red and yellow, corresponding to the pressure exerted by the screws and the crankshaft respectively. Homogeneous Neumann boundary conditions are imposed on the rest of the boundary

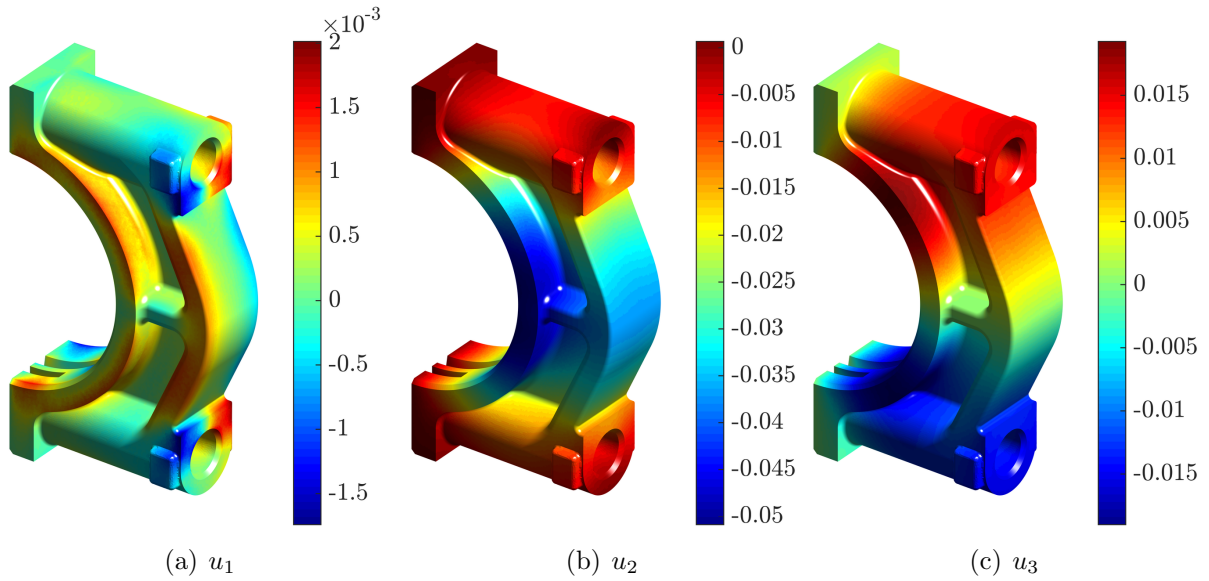


Figure 19: Bearing cap: components of the displacement field in mm.

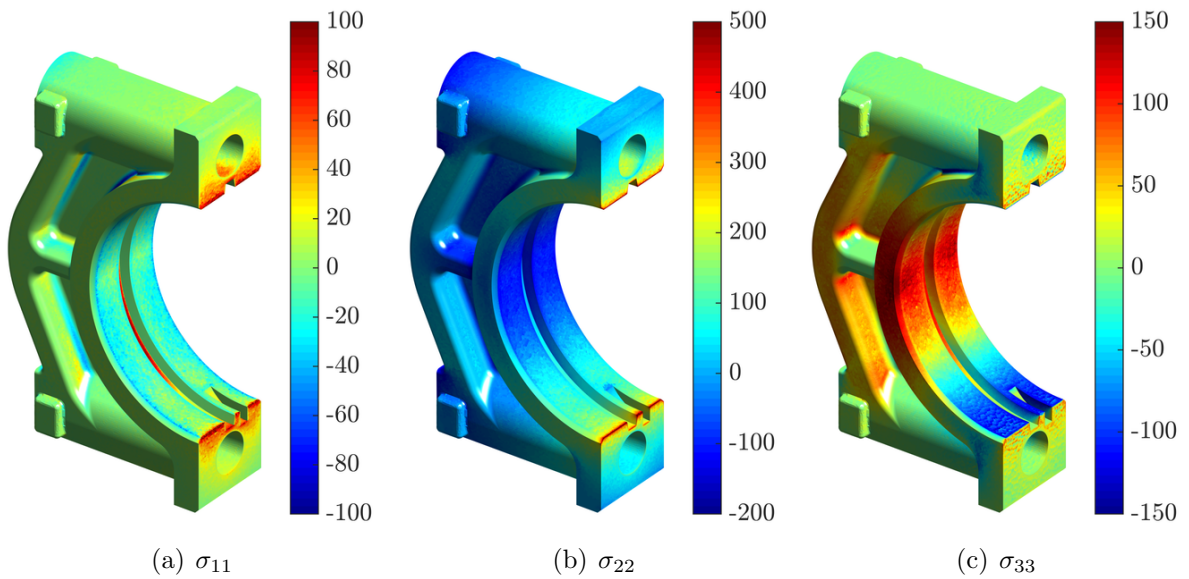


Figure 20: Bearing cap: three components of the stress field in  $\text{N}/\text{mm}^2$ .

surfaces in green. The bearing cap is made of cast iron with  $E = 130\text{GPa}$  and  $\nu = 0.25$ .

The three components of the computed displacement field and the axial components of the computed stress field are represented in Figures 19 and 20 respectively. The computation has been performed on an unstructured mesh with 2,398,627 tetrahedral elements. The mesh has 4,256,488 internal faces and 1,081,532 external faces, leading to a global



system with 15,854,985 degrees of freedom. The computation with the proposed FCFV method required 50 seconds to compute all elemental matrices, 23 seconds to perform the assembly of the global system and 41 hours to solve the system using a conjugate gradient method with no pre-conditioner. The developed code is written in Matlab and the computation was performed in an Intel<sup>®</sup> Xeon<sup>®</sup> CPU @ 3.70GHz and 32GB main memory available.

## 6 Concluding remarks

A new finite volume paradigm, based on the hybridisable discontinuous Galerkin (HDG) method with constant degree of approximation, has been presented for the solution of linear elastic problems. Similar to other HDG methods, the proposed face-centred finite volume (FCFV) method provides a volumetric locking-free approach. Contrary to other HDG methods, the symmetry of the stress tensor is strongly enforced using the Voigt notation, leading to optimal convergence of the stress field components.

The proposed FCFV method defines the displacement unknowns on the faces (edges in two dimensions) of the mesh elements. The displacement and stress fields on each element are then recovered using closed form expressions, leading to an efficient methodology that does not require a reconstruction of the gradient of the displacement and, therefore, it is insensitive to mesh distortion.

Numerical examples in two and three dimensions have been used to demonstrate the optimal convergence of the proposed method, its robustness when distorted meshes are considered and the absence of locking in the incompressible limit. The examples include classical benchmark test cases as well as a realistic application in three dimensions.

## Acknowledgements

This work is partially supported by the European Union's Horizon 2020 research and innovation programme under the Marie Skłodowska-Curie Actions (Grant number: 675919) and the Spanish Ministry of Economy and Competitiveness (Grant number: DPI2017-85139-C2-2-R). The first author also gratefully acknowledges the financial support provided by the Sêr Cymru National Research Network for Advanced Engineering and Materials (Grant number: NRN045). The second and third authors are also grateful for the financial support provided by the Generalitat de Catalunya (Grant number: 2017-SGR-1278).

## References

- [1] Ferdinando Auricchio, L Beirao da Veiga, Carlo Lovadina, and Alessandro Reali. An analysis of some mixed-enhanced finite element for plane linear elasticity. *Computer Methods in Applied Mechanics and Engineering*, 194(27-29):2947–2968, 2005.
- [2] C. Bailey and M. Cross. A finite volume procedure to solve elastic solid mechanics problems in three dimensions on an unstructured mesh. *International Journal for Numerical Methods in Engineering*, 38(10):1757–1776, 1995.
- [3] James R Barber. *Elasticity*. Springer, 2002.
- [4] I Bijelonja, I Demirdžić, and S Muzaferija. A finite volume method for incompressible linear elasticity. *Computer Methods in Applied Mechanics and Engineering*, 195(44-47):6378–6390, 2006.
- [5] D. Boffi, F. Brezzi, and M. Fortin. Reduced symmetry elements in linear elasticity. *Communications on Pure and Applied Analysis*, 8(1):95–121, 2009.
- [6] F. Brezzi and M. Fortin. *Mixed and hybrid finite elements methods*. Springer series in computational mathematics. Springer-Verlag, 1991.
- [7] Philip Cardiff, Željko Tuković, Hrvoje Jasak, and Alojz Ivanković. A block-coupled finite volume methodology for linear elasticity and unstructured meshes. *Computers & Structures*, 175:100–122, 2016.
- [8] Bernardo Cockburn, Bo Dong, and Johnny Guzmán. A superconvergent LDG-hybridizable Galerkin method for second-order elliptic problems. *Mathematics of Computation*, 77(264):1887–1916, 2008.
- [9] Bernardo Cockburn, Jayadeep Gopalakrishnan, and Raytcho Lazarov. Unified hybridization of discontinuous Galerkin, mixed, and continuous Galerkin methods for second order elliptic problems. *SIAM Journal on Numerical Analysis*, 47(2):1319–1365, 2009.
- [10] R.D. Cook, D.S. Malkus, M.E. Plesha, and R.J. Witt. *Concepts and applications of finite element analysis*. Wiley, 2002.
- [11] I. Demirdžić and S. Muzaferija. Finite volume method for stress analysis in complex domains. *International Journal for Numerical Methods in Engineering*, 37(21):3751–3766, 1994.
- [12] Boris Diskin and James L. Thomas. Accuracy of gradient reconstruction on grids with high aspect ratio. Technical report, NASA Langley Research Center, 2008.

- [13] Boris Diskin and James L. Thomas. Effects of mesh irregularities on accuracy of finite-volume discretization schemes. In *50th AIAA Aerospace Sciences Meeting and Exhibit; 9-12 Jan. 2012; Nashville, TN; United States*, 2008.
- [14] Boris Diskin and James L Thomas. Comparison of node-centered and cell-centered unstructured finite-volume discretizations: inviscid fluxes. *AIAA journal*, 49(4):836–854, 2011.
- [15] Boris Diskin, James L Thomas, Eric J Nielsen, Hiroaki Nishikawa, and Jeffery A White. Comparison of node-centered and cell-centered unstructured finite-volume discretizations: viscous fluxes. *AIAA journal*, 48(7):1326, 2010.
- [16] J. Fainberg and H.-J. Leister. Finite volume multigrid solver for thermo-elastic stress analysis in anisotropic materials. *Computer Methods in Applied Mechanics and Engineering*, 137(2):167 – 174, 1996.
- [17] N. Fallah. A cell vertex and cell centred finite volume method for plate bending analysis. *Computer Methods in Applied Mechanics and Engineering*, 193(33):3457 – 3470, 2004.
- [18] Jacob Fish and Ted Belytschko. *A First Course in Finite Elements*. John Wiley & Sons, 2007.
- [19] B.M. Fraeijs de Veubeke. Stress function approach. Proceedings of the world congress on finite element methods in structural mechanics, Rapport du LTAS, Universit de Lige, <http://hdl.handle.net/2268/205875>, 1975.
- [20] G. Fu, B. Cockburn, and H. Stolarski. Analysis of an HDG method for linear elasticity. *International Journal for Numerical Methods in Engineering*, 102(3-4):551–575, 2015.
- [21] Arun L Gain, Cameron Talischi, and Glaucio H Paulino. On the virtual element method for three-dimensional linear elasticity problems on arbitrary polyhedral meshes. *Computer Methods in Applied Mechanics and Engineering*, 282:132–160, 2014.
- [22] Jibrán Haider, Chun Hean Lee, Antonio J. Gil, Antonio Huerta, and Javier Bonet. An upwind cell centred Total Lagrangian finite volume algorithm for nearly incompressible explicit fast solid dynamic applications. *Computer Methods in Applied Mechanics and Engineering*, 2018. to appear.
- [23] H. Jasak and H. G. Weller. Application of the finite volume method and unstructured meshes to linear elasticity. *International Journal for Numerical Methods in Engineering*, 48(2):267–287, 2000.
- [24] Eirik Keilegavlen and Jan Martin Nordbotten. Finite volume methods for elasticity with weak symmetry. *International Journal for Numerical Methods in Engineering*, 112(8):939–962, 2017.

- [25] Chun Hean Lee, Antonio J Gil, and Javier Bonet. Development of a cell centred upwind finite volume algorithm for a new conservation law formulation in structural dynamics. *Computers & Structures*, 118:13–38, 2013.
- [26] P. W. McDonald. The computation of transonic flow through two-dimensional gas turbine cascades. In *ASME 1971 International Gas Turbine Conference and Products Show*, number 71-GT-89 in ASME. Turbo Expo: Power for Land, Sea, and Air, page V001T01A089, 1971.
- [27] A. Montlaur, S. Fernández-Méndez, and A. Huerta. Discontinuous Galerkin methods for the Stokes equations using divergence-free approximations. *International Journal for Numerical Methods in Fluids*, 57(9):1071–1092, 2008.
- [28] N. C. Nguyen, J. Peraire, and B. Cockburn. An implicit high-order hybridizable discontinuous Galerkin method for linear convection-diffusion equations. *Journal of Computational Physics*, 228(9):3232–3254, 2009.
- [29] N. C. Nguyen, J. Peraire, and B. Cockburn. An implicit high-order hybridizable discontinuous Galerkin method for nonlinear convection-diffusion equations. *Journal of Computational Physics*, 228(23):8841–8855, 2009.
- [30] N. C. Nguyen, J. Peraire, and B. Cockburn. An implicit high-order hybridizable discontinuous Galerkin method for the incompressible Navier-Stokes equations. *Journal of Computational Physics*, 230(4):1147–1170, 2011.
- [31] N.C. Nguyen, J. Peraire, and B. Cockburn. A hybridizable discontinuous Galerkin method for Stokes flow. *Computer Methods in Applied Mechanics and Engineering*, 199(9-12):582–597, 2010.
- [32] J. Nordbotten. Convergence of a cell-centered finite volume discretization for linear elasticity. *SIAM Journal on Numerical Analysis*, 53(6):2605–2625, 2015.
- [33] Jan Martin Nordbotten. Cell-centered finite volume discretizations for deformable porous media. *International Journal for Numerical Methods in Engineering*, 100(6):399–418, 2014.
- [34] W. Pan, M.A. Wheel, and Y. Qin. Six-node triangle finite volume method for solids with a rotational degree of freedom for incompressible material. *Computers & Structures*, 88(23):1506 – 1511, 2010.
- [35] A. W. Rizzi and M. Inouye. Time-split finite-volume method for three-dimensional blunt-body flow. *AIAA Journal*, 11(11):1478–1485, 2017/07/23 1973.
- [36] R. Sevilla, M. Giacomini, and A. Huerta. A face-centred finite volume method for second-order elliptic problems. *International Journal for Numerical Methods in Engineering*, (0):1–29, 2018.

- [37] R. Sevilla, M. Giacomini, A. Karkoulas, and A. Huerta. A super-convergent hybridizable discontinuous Galerkin method for linear elasticity. *International Journal for Numerical Methods in Engineering*, Under review, 2018.
- [38] R. Sevilla and A. Huerta. HDG-NEFEM with degree adaptivity for Stokes flows. *Journal of Scientific Computing*, 2018. To appear.
- [39] Ruben Sevilla and Antonio Huerta. Tutorial on Hybridizable Discontinuous Galerkin (HDG) for second-order elliptic problems. In J. Schröder and P. Wriggers, editors, *Advanced Finite Element Technologies*, volume 566 of *CISM International Centre for Mechanical Sciences*, pages 105–129. Springer International Publishing, 2016.
- [40] A.K. Slone, C. Bailey, and M. Cross. Dynamic solid mechanics using finite volume methods. *Applied Mathematical Modelling*, 27(2):69 – 87, 2003.
- [41] S-C Soon, B Cockburn, and Henryk K Stolarski. A hybridizable discontinuous Galerkin method for linear elasticity. *International Journal for Numerical Methods in Engineering*, 80(8):1058–1092, 2009.
- [42] R. Suliman, O.F. Oxtoby, A.G. Malan, and S. Kok. An enhanced finite volume method to model 2D linear elastic structures. *Applied Mathematical Modelling*, 38(7):2265 – 2279, 2014.
- [43] Barna Aladar Szabo and Ivo Babuška. *Finite element analysis*. John Wiley & Sons, 1991.
- [44] Stephen P Timoshenko and James N Goodier. *Theory of elasticity*, volume 3. McGraw-Hill, New York London, 1970.
- [45] Stephen P Timoshenko and Sergius Woinowsky-Krieger. *Theory of plates and shells*. McGraw-hill, 1959.
- [46] P Wenke and MA Wheel. A finite volume method for solid mechanics incorporating rotational degrees of freedom. *Computers & Structures*, 81(5):321–329, 2003.
- [47] M.A. Wheel. A finite-volume approach to the stress analysis of pressurized axisymmetric structures. *International Journal of Pressure Vessels and Piping*, 68(3):311 – 317, 1996.
- [48] M.A. Wheel. A finite volume method for analysing the bending deformation of thick and thin plates. *Computer Methods in Applied Mechanics and Engineering*, 147(1):199 – 208, 1997.
- [49] G. H. Xia, Y. Zhao, J. H. Yeo, and X. Lv. A 3d implicit unstructured-grid finite volume method for structural dynamics. *Computational Mechanics*, 40(2):299, Jul 2006.